



Three-Dimensional random network of metacomposites by synergizing Multi-Walled carbon Nanotube-Carbon black for tunable Epsilon-Negative and Epsilon-Near-Zero responses

Yunpeng Qu^a, Yunlei Zhou^{b,*}, Farid Manshahi^c, Kaidong Wang^c, Chunyuan Deng^{d,*}, Yao Liu^{e,*}

^a College of Physics, Guizhou University, Guiyang 550025, China

^b Hangzhou Institute of Technology, Xidian University, Hangzhou 311231, China

^c Department of Bioengineering, University of California, Los Angeles, Los Angeles, CA, 90095, United States

^d School of Electronic Engineering and Automation, Guilin University of Electronic Technology, Guilin 541004, China

^e Key Laboratory for Liquid-Solid Structural Evolution and Processing of Materials (Ministry of Education), Shandong University, Jinan 250061, China

ARTICLE INFO

Keywords:

Metacomposites

A. Polymer-matrix composites

B. Microstructures

B. Electrical properties

ABSTRACT

Epsilon-near-zero (ENZ) and epsilon-negative (EN) responses are remarkable properties of electromagnetic (EM) metamaterials that have sparked considerable interest. This paper introduces an innovative strategy using ternary metacomposites that achieve excellently tunable ENZ ($|\epsilon'| < 1$) and EN ($\epsilon' < 0$) parameters within the radio-frequency band. The approach leverages a synergistic effect of multi-walled carbon nanotube-carbon black (MWCNT-CB) composites integrated into a polyaniline (PANI) matrix to construct three-dimensional (3D) carbon networks. As the loading content of MWCNT-CB increases, these networks evolve from clusters, enabling a finely tunable range of EN parameters from 10^0 to 10^3 . The ENZ response occurs at approximately 265 MHz and 830 MHz, triggered by dielectric resonance due to electric dipoles at MWCNT-CB/PANI interfaces and a low-frequency plasmonic state in the 3D MWCNT-CB networks, respectively. This research establishes a foundation for tunable ENZ and EN responses by introducing a new class of ternary metacomposites.

1. Introduction

In recent years, epsilon-near-zero (ENZ) and epsilon-negative (EN) metamaterials have captured widespread interest due to their exceptional capabilities, such as perfect electromagnetic (EM) interference shielding, the creation of *meta*-capacitors with colossal dielectric constants, and negative refraction [1–4]. Initially, ENZ ($|\epsilon'| < 1$) and EN ($\epsilon' < 0$) parameters were achieved through artificial media consisting of periodic metallic wires and rings [4,5]. Subsequently, a variety of periodic structures were developed to facilitate tunable ENZ and EN responses for applications like invisible cloaks, *meta*-lens, and reversed Doppler effects [6,7]. By meticulously tailoring the geometrical configurations on a subwavelength scale, including structures like split-ring resonators, wires, fishnets, or cut-wire pairs, these metamaterials have been adapted to meet practical needs [3–7]. However, their success or failure hinges on a common attribute of the metamaterials, which often complicates manufacturing and hinders multifunctional integration,

thus limiting their range of applications [8,9].

This limitation is beginning to be addressed by shifting metamaterial design towards more random structures, such as percolated composites containing randomly distributed building blocks [9–11]. Known as metacomposites, this type of material focuses on the intrinsic properties of the components rather than relying on periodic units [9–11]. Employing randomly distributed building blocks, metacomposites offer a significant amount of design freedom [12]. For instance, conventional metals (Fe, Ni, Cu, and Ag) can be incorporated into insulating matrices to create 3D networks that exhibit ENZ and EN responses at specific frequency ranges [13–16]. The negative parameters are fine-tuned by optimizing the chemical composition and the structure of the random composites. Metals are often paired with ceramic matrices due to their effective and straightforward manufacturing processes [17]. Importantly, this metacomposite approach allows for the dilution of the metals' equivalent electron concentration, enabling intrinsic plasmonic states to respond at radio frequencies instead of the optical band [18].

* Corresponding authors.

E-mail addresses: zhouyunlei@xidian.edu.cn (Y. Zhou), dcy0606dcy@163.com (C. Deng), liuyao@sdu.edu.cn (Y. Liu).

<https://doi.org/10.1016/j.compositesa.2024.108410>

Received 13 May 2024; Received in revised form 16 July 2024; Accepted 13 August 2024

Available online 15 August 2024

1359-835X/© 2024 Elsevier Ltd. All rights are reserved, including those for text and data mining, AI training, and similar technologies.

This strategy offers a new avenue for achieving ENZ and EN responses but also presents challenges in precisely regulating performance [19].

Interestingly, recent advancements have focused on carbon/polymer systems for ENZ and EN responses, potentially overcoming the limitations faced by metal/ceramic metacomposites such as high loss, severe frequency dispersion, and difficulty in lightweighting [20–22]. Carbon nanomaterials, such as carbon nanotubes (CNT), graphene (GR), and carbon black (CB), exhibit impressive physical properties including moderate equivalent electron concentration, controllable geometric configuration, and stability under various physical conditions [23–27]. Significant reports have highlighted the advantages of the carbon/polymer system due to their low density, low carrier concentration, and tunable physical properties [28–31]. However, experimental research on carbon/polymer metacomposites is still lacking, leaving the response mechanisms of ENZ and EN behaviors unclear [32–34]. There is a pressing need to focus on this type of metacomposite to elucidate these mechanisms and explore new strategies and branches.

Building on preliminary work with binary carbon/polymer metacomposites [35–37], we have taken further steps by fabricating a 3D network composed of multi-walled carbon nanotube-carbon black (MWCNT-CB) binary filler, embedded within a polyaniline (PANI) matrix. Due to the synergistic effects within the MWCNT-CB network, the dielectric performance can be precisely tuned which can avoid the limitation that EN response characteristics can only be controlled by a single carbon functional phase in the previous binary metacomposites [10–12]. MWCNT provides a long-range carrier conductive channel, while CB offers a low carrier concentration. PANI was specifically chosen as the matrix material due to its adjustable electrically conductive properties, which can further regulate the ENZ and EN responses. Additionally, the electrical conduction mechanism, dielectric loss performance, and impedance characteristics of the MWCNT-CB/PANI metacomposites are investigated, providing comprehensive insights into this innovative material system.

2. Results and Discussion

2.1. Structural and Compositional characterization

In what follows, we provide a comprehensive characterization of the microstructures, morphologies, and thermal performance of MWCNT-CB/PANI metacomposites and their component materials. The fabrication process of MWCNT-CB/PANI ternary metacomposites is schematic in Fig. 1a, b, and the detailed description is shown in the section 1 in Supplementary Material. As depicted in Fig. 2a–e, the one-dimensional (1D) MWCNTs, characterized by a large aspect ratio, and the zero-dimensional (0D) CBs, noted for their low carrier concentration, form a grape-like structure via a one-step electrostatic self-assembly process. In this configuration, the MWCNTs serve as efficient conductive pathways while the CB acts as a tuning phase for carrier concentration and a protector of the conductive networks within the PANI matrix [10–12]. The FESEM images (Fig. S1a–i) clearly show that the functional phases of MWCNT-CB are randomly distributed, contrasting with the EN and ENZ responses achieved by designing regular periodic functional phases in array metamaterials. Additionally, the simplicity of the self-assembly process for creating these grape-shaped binary functional phases is further illustrated in the TEM images (Fig. S1a–o), offering new insights into the design of functional phases for EN metamaterials and metacomposites [15–17].

Attention to the morphology of the PANI powders reveals that the polymer, synthesized through aniline polymerization, assumes an irregular cluster shape as seen in Fig. 2f–j and Fig. S3a–e. Although the electrical and dielectric properties of the MWCNT-CB and PANI powders cannot be determined through micro-ordered structures, the ratio of functional to matrix phases can be quantitatively designed according to the percolation criterion during the construction of the metacomposites.

We have constructed a series of MWCNT-CB/PANI composites with

varying MWCNT-CB content from 2 wt% to 14 wt%. This variation in filler content triggers an evolution of microstructure, specifically transitioning from isolated carbon cluster structures to three-dimensional (3D) carbon network composed of MWCNT-CB filler. The integrity of the grape-like MWCNT-CB functional phase prepared by electrostatic self-assembly process is due to the process of pre synthesizing MWCNT-CB binary functional phase and then physically milling it and dispersing it with PANI matrix. The FESEM images in Fig. 3a–g show that at 2 wt%, the MWCNT-CB fillers exhibit cluster aggregation within the PANI matrix and gradually increase contact with each other as their content rises from 4 wt% and 14 wt%, progressively forming a more robust 3D carbon network. Despite potential gaps of about 300 nm when the MWCNT-CB content is high, the large aspect ratio of the grape-shaped functional phase ensures that the 3D conductive network effectively bridges these gaps, thus maintaining the structural and electrical stability of the composites (Fig. S4a–l and Fig. S4a–i).

The composition of the as-prepared MWCNT-CB/PANI composites remains consistent, evidenced by the absence of impurities in their XRD patterns shown in Fig. 3h. The XRD analysis of pure PANI reveals several weak crystallization peaks, between 20° and 20° , indicative of the periodic arrangement of the polymer chains. The MWCNT-CB fillers, due to their low content and weak diffraction peaks, are less discernible and are encased within the PANI network. Selected samples of pure PANI and 10 wt% MWCNT-CB/PANI were analyzed using Raman, FT-IR, and TG-DSC, as displayed in Fig. 3i–l. The RAMAN spectroscopy results indicate that pure PANI exhibits peaks at 2850 cm^{-1} , 1580 cm^{-1} , and 1347 cm^{-1} , corresponding to carbon hybridization and vibrations of C=C and C-H bonds [30]. The 10 wt% MWCNT-CB/PANI composite shows a weaker peak at 2850 cm^{-1} and an additional peak at 1170 cm^{-1} , indicating enhanced C=C bond interactions within the MWCNT-CB fillers [31,32]. The incorporation also alters the transmittance, particularly in the $2000\text{--}500\text{ cm}^{-1}$ range, with the formation of the MWCNT-CB network effectively blocking electromagnetic wave propagation. The TG-DSC curves (Fig. 3k–l) for both pure PANI and the MWCNT-CB/PANI composites exhibit similar trends upon heating to 1000°C in air, with rapid endothermic reactions occurring between $\sim 250^\circ\text{C}$ and $\sim 700^\circ\text{C}$ due to high-temperature decomposition of PANI and MWCNT-CB, illustrating that the presence of MWCNT-CB prolongs the heat absorption process.

2.2. Electrical properties

After examining the microstructures and compositions, we next explore the electrical properties of the MWCNT-CB/PANI metacomposites. As displayed in Fig. 4a, the AC conductivity (σ_{ac}) of all samples generally exhibits a decreasing trend across the entire test frequency range (20 MHz–1 GHz), except for the 2 wt% composites. This particular sample demonstrates a slight increase in conductivity in the lower frequency range (20 MHz–265 MHz), which can be attributed to Jonscher's power law: [32–34]

$$\sigma_{ac} = \sigma_{dc} + A(2\pi f)^n \quad (1)$$

where σ_{dc} represents the direct current conductivity, f denotes the test frequency, A is the pre-exponential factor, and n is the fractional exponent ($0 < n < 1$). This upward trend below the ENZ frequency reflects the hopping conduction behavior typically seen in dielectrics with positive permittivity. Beyond the ENZ frequency (265 MHz), the σ_{ac} of the 2 wt% composites begin the decline due to the skin effect, which is described by the Drude model: [35,36]

$$\sigma_{ac} = \frac{\sigma_{dc}\omega_\tau^2}{(2\pi f)^2 + \omega_\tau^2} \quad (2)$$

$$\sigma_{dc} = \frac{Ne^2\tau}{m} = \frac{\omega_p^2\tau}{4\pi} \quad (3)$$

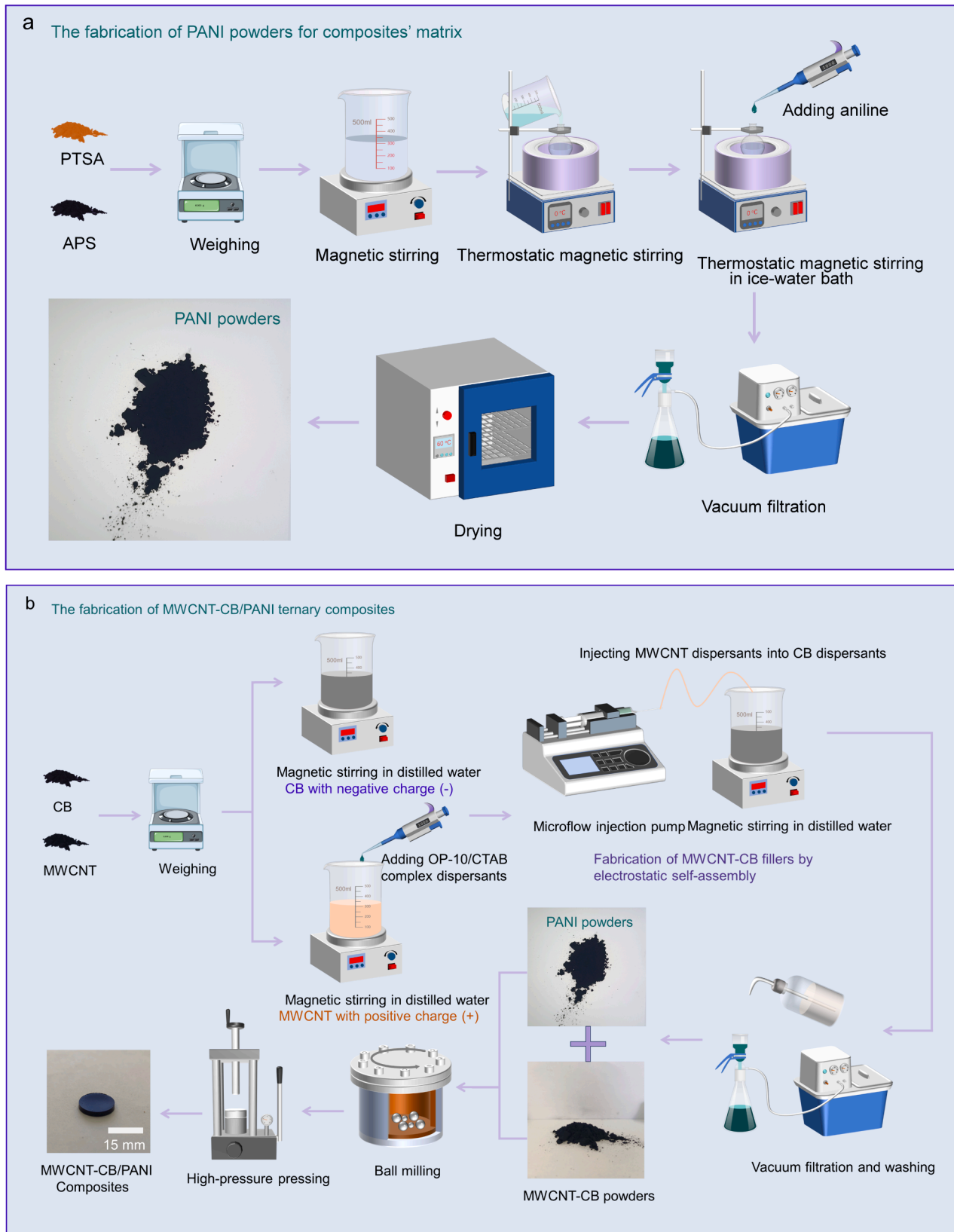


Fig. 1. Schematic illustration of the fabrication process: (a) synthesis of PANI powders and (b) one-step electrostatic self-assembly, ball-milling, and high-pressure pressing to create MWCNT-CB/PANI ternary composites.

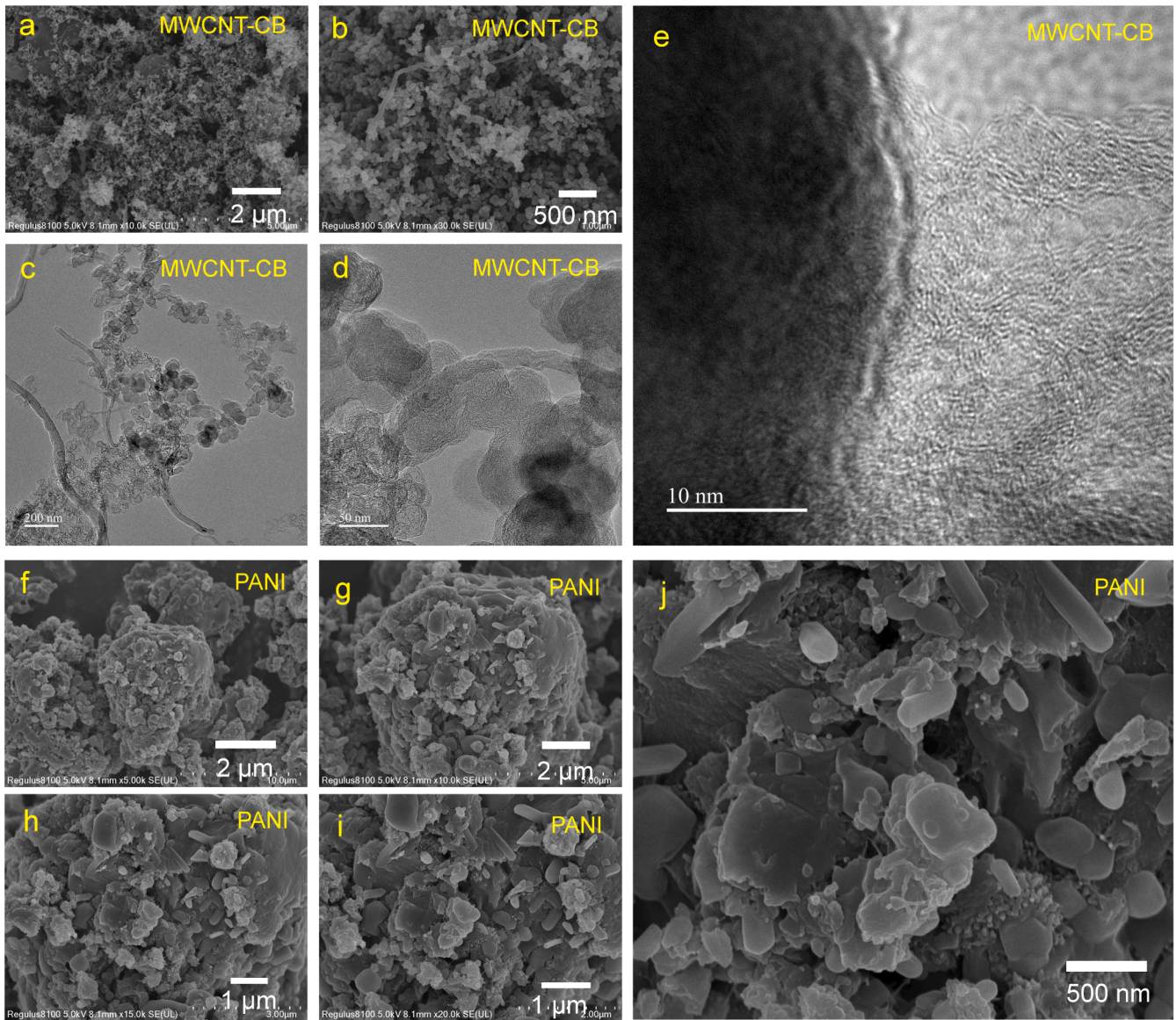


Fig. 2. FESEM and TEM images of (a-e) MWCNT-CB powders and (f-j) PANI powders.

here, ω_τ ($\omega_\tau = 1/\tau$) is the relaxation rate, ω_p ($\omega_p = 2\pi f_p$) is the plasma frequency, e is the electron charge ($1.6 \times 10^{-19}\text{C}$), N is the Avogadro constant, and m is the electron mass. These results suggest a metal-like conduction behavior with variable skin depth. The dashed lines in Fig. 4a illustrate the theoretical predictions according to the Drude model. The discrepancy between the theoretical predictions and the experimental σ_{ac} values stems from the fact that the MWCNT-CB/PANI metacomposites we constructed are a random heterogeneous structure. When the applied electric field frequency exceeds 100 MHz, there is a divergence in the theoretical skin depth compared to that of pure metal materials. The quantified skin depth (δ) can be expressed as: [37,38]

$$\delta = \sqrt{\frac{2}{2\pi f \mu \sigma_{ac}}} \quad (4)$$

where μ indicates static permeability. Notably, the MWCNT-CB/PANI metacomposites exhibit a higher δ than the theoretical value, a common occurrence in composites. Despite the non-uniform distribution of the conductive network of MWCNT-CB within the PANI matrix, it does

not hinder our ability to achieve EN response through the network, since EN and ENZ responses are closely linked to the overall carrier concentration.

2.3. Epsilon-Negative and Epsilon-Near-Zero responses

As shown in Fig. 4b, the 2 wt% MWCNT-CB/PANI metacomposites successfully achieve EN and ENZ responses at high frequencies. Specifically, the ENZ frequency marks the point where the real permittivity (ϵ') transitions from a positive to a negative value around 265 MHz. This occurs because, at this stage, the MWCNT-CB has not yet formed a complete 3D network within the PANI matrix. Under the influence of the alternating electric field, numerous charge carriers are generated at the interfaces between MWCNT-CB and PANI, taking the form of electric dipoles and resulting in dielectric resonance. This behavior is well-described by the Lorentz model for the radio-frequency (RF) region: [39,40]

$$\epsilon' = 1 + \frac{\omega_p^2(\omega_0^2 - \omega^2)}{(\omega_0^2 - \omega^2)^2 + \omega^2\Gamma_L^2} \quad (5)$$

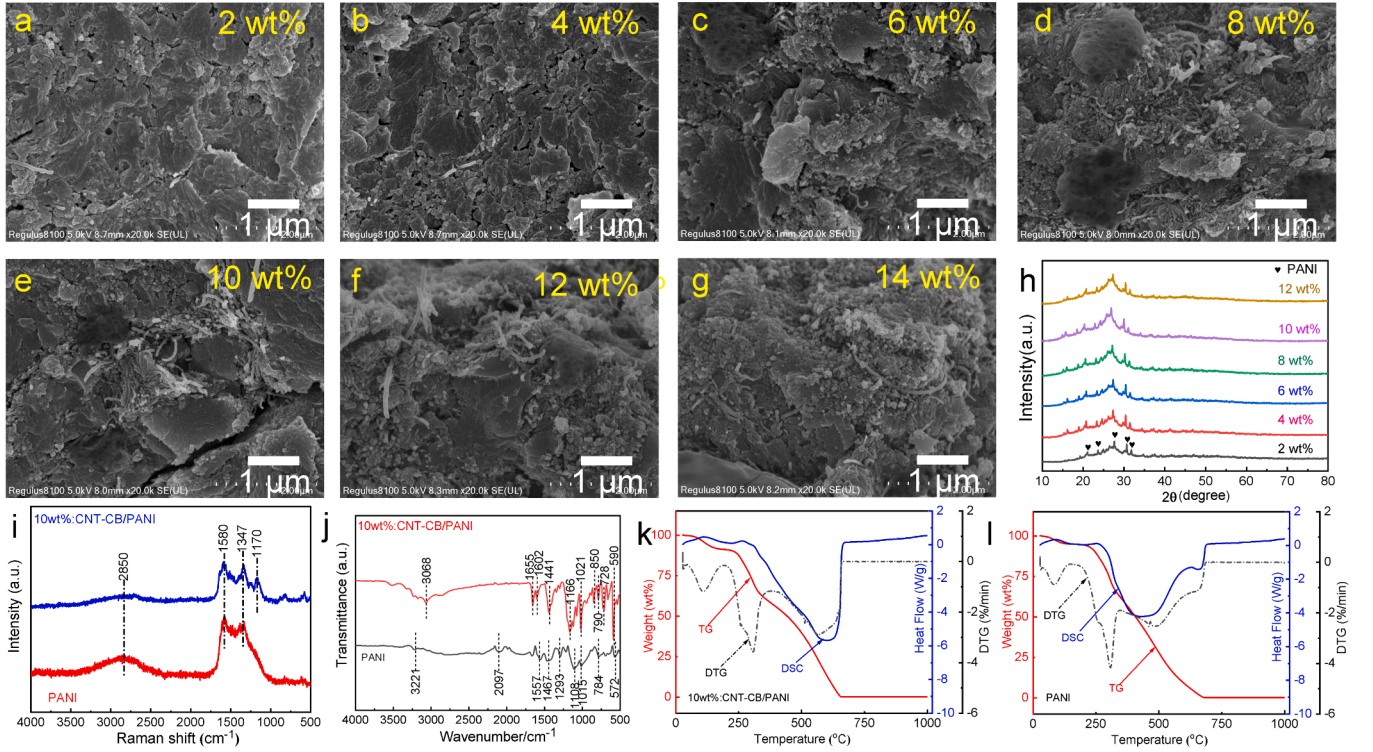


Fig. 3. (a-g) FESEM images displaying the internal cross-sectional morphologies of MWCNT-CB/PANI composites with increasing MWCNT-CB content, (h) XRD patterns, (i) Raman spectra, (j) FT-IR spectra, and (k-l) TG-DSC curves for both MWCNT-CB/PANI composites and PANI powders.

where ω ($\omega = 2\pi f$) is the frequency of the electric field, ω_0 is the resonance frequency, and Γ_L is the damping constant. The model closely matches the frequency dispersion of ϵ' for the 2 wt% MWCNT-CB/PANI metacomposites, as indicated by the dashed lines in Fig. 4b. The interface potential barrier and contact gap within the MWCNT-CB/PANI composites introduce a damping effect, causing the dielectric resonance to exhibit a gradual change with increasing frequency, which leads to a weak EN response in the range of 265 MHz-1 GHz, where the absolute value of ϵ' remains below 1000 ($|\epsilon'| < 1000$).

As the MWCNT-CB content increases, the formation of effective conductive pathways and the corresponding rise in carrier concentration change the nature of the carriers. Instead of existing as electric dipoles, they form a collective plasmonic oscillation under the excitation of an external alternating electric field, thus exhibiting an EN response across the RF spectrum. The 4 wt% metacomposites display a weak EN response from about 20 MHz to 830 MHz, with the ENZ response occurring around ~ 830 MHz (Fig. 4b). This is distinct from the 2 wt% composites, as ϵ' for the 4 wt% metacomposites shifts from a negative value to a positive value. This Drude model explains this type of EN and ENZ responses: [41,42]

$$\epsilon' = \epsilon_\infty - \frac{\omega_p^2}{\omega^2 + \Gamma_D^2} \quad (6)$$

$$\omega_p = \sqrt{\frac{n_{\text{eff}} e^2}{m_{\text{eff}} \epsilon_0}} \quad (7)$$

$$f_\Omega = \frac{f_p}{\sqrt{\epsilon_\infty}} \quad (8)$$

here, ϵ_0 is the vacuum permittivity (8.85×10^{-12} F/m), ϵ_∞ represents the high-frequency limit permittivity, Γ_D is the damping constant, n_{eff} and m_{eff} are the effective concentration and mass of free carriers, respectively, and f_Ω is the screened plasma frequency. The EN response is

expected when the frequency is below f_Ω , explaining the observed ENZ response of the 4 wt% metacomposites. With further increases in MWCNT-CB content, a consistent EN response is achieved across the entire test frequency band, marked by a stable ϵ' value between -600 and -50 . This is attributable to the enhanced effective carrier concentration n_{eff} within the robust 3D MWCNT-CB network. The dashed lines in Fig. 4b represent the Drude model fittings. Notably, the EN response of metacomposites with 2-6 wt% MWCNT-CB content was classified as weakly negative ($|\epsilon'| < 1000$).

To further explore the regulation of EN response, we developed metacomposites with higher MWCNT-CB contents, and their ϵ' spectra are displayed in Fig. 4c. The EN responses of these 8-14 wt% metacomposites align with the Drude model, showing an increasing trend as the test frequency increases. The dashed lines represent the fitting results from the Drude model. No ENZ behavior is observed at this stage, as the carrier concentration within the metacomposites is sufficiently high, resulting in a f_Ω that is higher than the test frequency band. This allows us to achieve a wideband EN response in the RF region. For instance, at 20 MHz, the EN response of the MWCNT-CB/PANI metacomposites can be stably regulated to values such as 2000, 3000, 4000, and 6000. In the high-frequency testing range, near 1 GHz, the EN response magnitude of all metacomposites tends to stabilize. This occurs because, at higher frequencies, the plasmonic oscillation frequency of the numerous free charge carriers within the material cannot respond quickly enough, leading to a uniform EN response level across metacomposites with varying carrier concentrations. A significant observation is that the magnitude of EN response achieved through our specially designed 3D MWCNT-CB collaborative carbon network is reduced by at least 3-4 orders of magnitude compared to traditional metal-based metamaterials and metacomposites, as shown in Table 1. In this part of the work, we focus on the synergistic effect of MWCNT-CB dual functional phase on EN response. Composite materials with MWCNT or CB as a single functional phase will be the focus of our future research.

In addition to studying the EN and ENZ response characteristics of metacomposites, it is crucial to examine their loss characteristics in

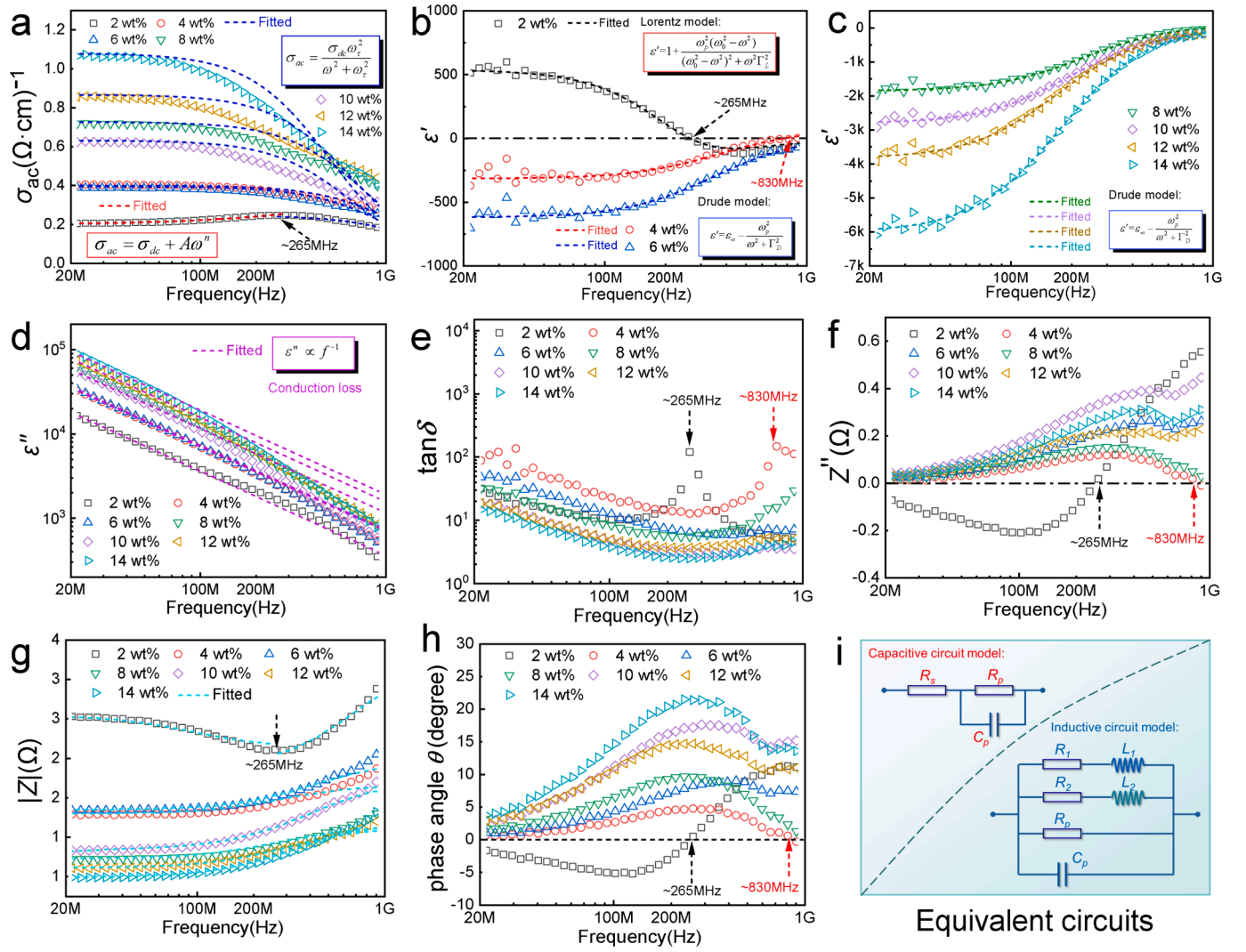


Fig. 4. (a) Frequency dependences of AC conductivity, (b-d) complex permittivity, (c) loss tangent angle, (f) reactance, (g) impedance modulus, with dash lines representing fitting results from equivalent circuit analysis, and (h) phase angle measurements for MWCNT-CB/PANI composites. (i) Schematic of equivalent circuit used for analysis.

detail. The imaginary part of permittivity (ϵ'') and loss tangent angle ($\tan \delta = |\epsilon''/\epsilon'|$) of the MWCNT-CB/PANI metamaterials are used to characterize their dielectric loss properties, as illustrated in Fig. 4d-e. Throughout the testing frequency range, ϵ'' shows a significant downward trend, primarily due to conduction loss (ϵ_C''). For metamaterials with lower MWCNT-CB content, ϵ_C'' generally dominates across the entire testing frequency band, as displayed by the dashed lines in Fig. 4d. However, for those with higher MWCNT-CB content, deviations between ϵ'' and ϵ_C'' at high frequencies are observed, attributable to dipolar loss (ϵ_D'') and losses related to interfacial polarization (ϵ_P''). This behavior is intricately linked to the heterogeneous structural characteristics of the metamaterials. Despite the formation of the MWCNT-CB network within the material, significant charge accumulation occurs at the interfaces between MWCNT-CB and PANI. This accumulation results in interface polarization and electric dipole movement, leading to energy loss. Especially at high frequencies, the skin effect can cause an uneven internal current distribution within the material, which in turn results in an ϵ'' value exceeding the theoretical ϵ_C'' . The ϵ_C'' mainly stems from the leakage current within the MWCNT-CB network and can be described by the equation: [43,44]

$$\epsilon_C'' = \frac{\sigma_{dc}}{2\pi f \epsilon_0} \quad (9)$$

where σ_{dc} is constant for each MWCNT-CB/PANI metamaterial, making ϵ_C'' inversely proportional to the f . For a more accurate representation of the ϵ'' spectrum, we incorporate the measured σ_{ac} of the metamaterials into the formula for ϵ_C'' : [45,46]

$$\epsilon_C'' = \sigma_{ac}/2\pi f \epsilon_0$$

The $\tan \delta$ spectra of the MWCNT-CB/PANI metamaterials, as shown in Fig. 4d, present loss peaks at ~265 MHz and ~830 MHz for ENZ media. These peaks suggest fluctuations in energy during transitions between positive and negative values of ϵ'' . This change directly relates to the dynamics of the free charge carriers within the metamaterials.

2.4. Equivalent circuit analysis

Building on the investigation of EN and ENZ responses in MWCNT-CB/PANI metamaterials, we extended our analysis to examine their impedance characteristics, as shown in Fig. 4f-h. A well-established relationship in dielectrics links the reactance (Z'') and permittivity (ϵ'), expressed as: [47,48]

$$\epsilon' = \frac{Z''}{2\pi f C_0 (Z^2 + Z'^2)} \quad (10)$$

Table 1
Summary of metamaterials with EN and ENZ responses.

Component classification	metacomposites	filler content	Magnitude of EN value	ENZ frequency	EN mechanism	Test frequency	Refs
Binary, Metal/ Ceramic	Ag/Si ₃ N ₄	34–50 wt%	-10 ³ ~ 0	7.4 GHz, 14.8 GHz	Plasma oscillation	2 GHz-18 GHz	[38]
	Ni/YIG	3.4–26.6 wt%	-10 ⁴ ~ -10 ¹	—	Plasma oscillation, Dielectric resonance	1 kHz-10 MHz	[39]
	Cu/TiO ₂	50–60 wt%	-10 ³ ~ -10 ²	—	Plasma oscillation	10 MHz-1 GHz	[40]
	Ni/YIG	40–60 wt%	-10 ⁴ ~ -10 ¹	—	Plasma oscillation	10 MHz-1 GHz	[41]
	Cu/TiO ₂	41.6–52.5 vol%	-10 ⁵ ~ -10 ³	—	Plasma oscillation	10 kHz-1 MHz	[43]
	GR/Al ₂ O ₃	2–8 wt%	-10 ⁶ ~ -10 ¹	—	Plasma oscillation	20 kHz-10 MHz	[44]
	C/Al ₂ O ₃	12.2–17.4 wt%	-10 ⁴ ~ -10 ¹	—	Plasma oscillation	20 MHz-1 GHz	[45]
	CF/Al ₂ O ₃	2–14 wt%	-10 ⁶ ~ 0	1660 Hz	Plasma oscillation	1 kHz-10 MHz	[46]
	GR/PS	30 wt%	-10 ¹ ~ 0	920 kHz	Plasma oscillation	10 kHz-1 MHz	[47]
	CNT/Epoxy MWCNT/PVDF	12–18 wt% 13–20 wt%	-10 ³ ~ -10 ² -10 ² ~ -10 ¹	— —	— —	Plasma oscillation Plasma oscillation	1 MHz-1 GHz 10 kHz-1 MHz
Ternary Metacomposites	CNTs/TiN _x /CCTO _y	1–8 wt%, x:y = 4:6	~ -10 ³ ~ 0	~600 MHz	Plasma oscillation	10 MHz-1 GHz	[31]
	C/CF/Epoxy	3.74–11.76 vol%	-10 ³ ~ -10 ²	—	Plasma oscillation	10 kHz-1 MHz	[50]
	(Cu _x /Cu@SiO ₂) _{0.7} /PVDF _{0.3} MWCNT-CB/PANI	x = 0.7–0.9 2–14 wt%	-10 ³ ~ -10 ² -10 ³ ~ 0	— 265 MHz, 830 MHz	— Plasma oscillation, Dielectric resonance	10 kHz-1 MHz 20 MHz-1 GHz	[51]

where C_0 represents the vacuum capacitance and Z' is resistance. Metacomposites with a positive ϵ' exhibit capacitive behavior, which can be derived from the formula: $Z'' = Z_L - Z_C$, where Z_L and Z_C represent inductive and capacitive reactance, respectively. Our findings indicate that the MWCNT-CB/PANI metacomposites act as a combination of a capacitor (C), inductor (L), and resistor (R). A negative Z'' value suggests that Z_C is less than Z_L , indicating the capacitive nature of the composites. For example, the 2 wt% metacomposites exhibit a negative Z'' below 265 MHz and transition to a positive value at higher frequencies, shifting from capacitive to inductive characteristics (Fig. 4f). This behavior offers the potential for designing frequency-controlled electronic components. In the case of 4 wt% metacomposites, a transition from electrical inductance to capacitance near ENZ frequency mirrors their EN response change. With increasing MWCNT-CB content, the metacomposites consistently show a positive Z'' across the test frequency range, indicating a predominant inductive character.

Through equivalent circuit analysis of the impedance characteristics, we can quantitatively describe the internal equivalent capacitance, inductance, and resistance of the metacomposites, as evidenced by the frequency dependences of the impedance modulus ($|Z|$) shown in Fig. 4g. For metacomposites with a positive ϵ' , the $|Z|$ is modeled using a circuit composed of resistors (R_s and R_p) and a capacitor (C_p), depicted in Fig. 4i. The phase angle (θ) values are correspondingly negative, indicating a lag in the voltage phase relative to the current phase, as shown in Fig. 4h. Conversely, at ENZ frequencies (265 MHz and 830 MHz), where θ approaches zero, the voltage and current are synchronized, showing near-pure resistive behavior.

For metacomposites displaying an EN response, an inductive character is modeled with circuits comprising inductors, as schematically shown in Fig. 4i. These metacomposites exhibit a varying electrical character and current–voltage phase relationship, with θ values being positive across the entire test frequency range (6–14 wt%), indicating that the voltage leads the current. Although the phase angle for pure inductors is 90 degrees, the angles we observed are typically below 20 degrees, suggesting the material possesses combined resistance and

inductance properties. This aligns with the 3D carbon network structure within the PANI matrix: the MWCNT-CB network mainly provides inductance, interfacial polarization at MWCNT-CB/PANI interfaces provides capacitance, and resistance is predominantly offered by the PANI matrix. In conclusion, the EN and ENZ media display contrasting electrical and dielectric properties, promising for applications such as precise EM wave control, innovative coil-less inductors, high-frequency metacapacitors, and ultra-sensitive sensors, among others [48,49].

2.5. EM shielding effectiveness and thermal performance

Utilizing the as-prepared MWCNT-CB/PANI metacomposites, we have successfully tailored the EN and ENZ response characteristics across the 20 MHz-1 GHz frequency range. Subsequently, we pay attention to simulation of the EM field and potential distribution which helps explaining the EN response mechanism inside metacomposites. Fig. 5a shows the synergistic effect of MWCNT-CB in achieving EN response. The long-range conductive pathways provided by MWCNT, combined with the moderate carrier concentrations from CB, enable tunable and weakly EN responses. Under high-frequency alternating electric fields, low-frequency plasma oscillations occur within the 3D random carbon network of the metacomposites [41,42]. The oscillations, when excited by an EM wave, generate fluctuations in charge density. Below the f_{Ω} , these fluctuations cause a sharp attenuation of the incident EM waves, demonstrating theoretically significant EM shielding effectiveness, as shown in Fig. 5b-g and Figure S6.

The distribution of the electric field vector is simulated using Computer Simulation Technology (CST) and COMSOL software. For example, 2 wt% metacomposites at 20 MHz, 265 MHz, and 1 GHz are shown in Fig. 5h-j. The EM waves are effectively blocked by the samples, attributed to the formation of the 3D MWCNT-CB networks. Once the EM waves penetrate these networks, an EM absorption effect is realized through conversion to conduction loss. As the MWCNT-CB content increases, the strength of the plasmonic state is enhanced, demonstrating near-perfect shielding effectiveness at 1 GHz (Figure S6).

It is important to note the differences in the mechanisms of EM

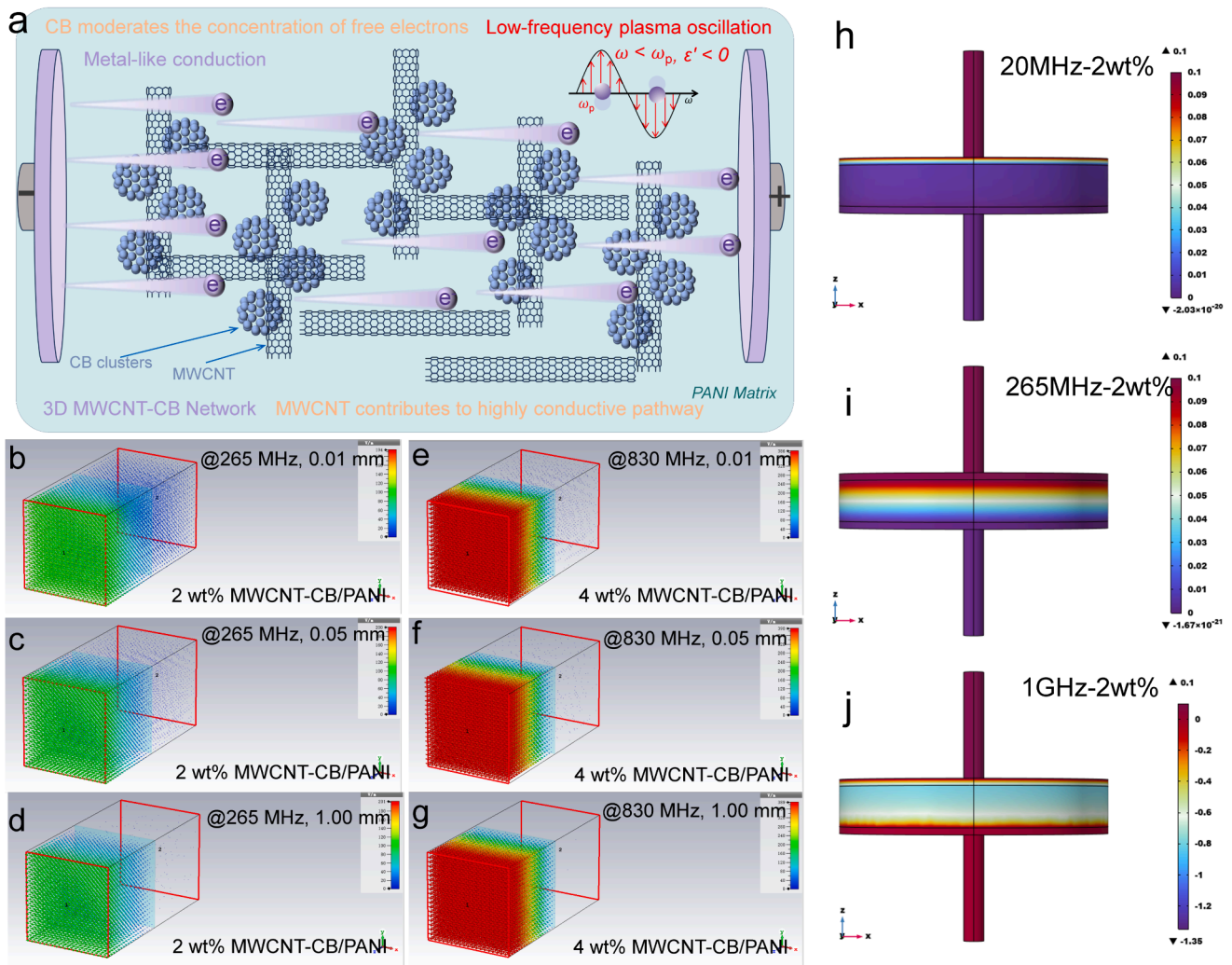


Fig. 5. (a) Schematic illustrating the EN response mechanism and microstructural evolution of MWCNT-CB fillers. (b-g) Electric field vector distribution at ENZ frequencies, highlighting variations in MWCNT-CB content and sample thickness. Potential distribution diagrams for 2 wt% MWCNT-CB composites at different frequencies (h) 20 MHz, (i) 265 MHz, and (j) 1 GHz, respectively.

shielding effectiveness between EN and ENZ media (Fig. 5h-j). For EN media, the main mechanism is the plasma oscillation state, which mainly reflects EM waves. Conversely, for ENZ media, it involves the perfect absorption of EM waves upon entry into the medium. In practical applications of these metamaterials, factors such as impedance matching characteristics, response frequency band, and response stability of EN and ENZ media must be comprehensively considered. Nonetheless, this research lays a foundational basis for designing new EM shielding devices based on EN and ENZ responsive metamaterials, highlighting promising application possibilities [43,44].

In typical electronic component applications, the heating problem of EM media is one of the key factors affecting their work efficiency and stability. Therefore, we further evaluated the thermal conductivity performance of metamaterials with EN response, as shown in Fig. 6a-p and Figure S7a-r. Sample of metamaterials with MWCNT-CB content of 14 wt% was heated at temperature of 60 °C, 80 °C, 100 °C and 120 °C. Obviously, after the formation of a 3D random carbon network in metamaterials, it is possible to form plasmonic oscillation behavior under the excitation of EM fields. Under the action of thermal fields, the main heat transfer carriers in MWCNT-CB are phonons rather than electrons. The perfect lattice structure and strong C-C covalent bonds between atoms of MWCNT result in a long average free path of phonons, leading to ultra-high thermal conductivity. Therefore, in comparison,

metamaterials with 14 wt% content of MWCNT-CB has a faster heating rate than those with 2 wt% content. Of course, in this part of our work, we have only explored the heat transfer performance of metamaterials initially. To gain a deeper understanding of their heat loss and radiation mechanism under high-frequency EM wave excitation, further research is needed. Nevertheless, our work will provide a research foundation for the application of EN and ENZ metamaterials in fields such as EM shielding, EM absorption, and metacapacitors [45,46,52].

3. Conclusion

Herein, the as-prepared MWCNT-CB/PANI ternary metamaterials demonstrated tunable ENZ and EN responses in the RF region, a development facilitated by the synergistic effect of MWCNT-CB within a PANI matrix. These 3D random carbon networks, which evolve from MWCNT-CB clusters as the loading content increases, allow for precise tuning order of the EN parameter from 10^0 to 10^3 . The ENZ responses at around 265 MHz and 830 MHz are triggered by distinct mechanisms: dielectric resonance, induced by electric dipoles at the MWCNT-CB/PANI interfaces, and a low-frequency plasmonic state within the 3D MWCNT-CB networks. Our equivalent circuit analysis has highlighted the inductive characteristics of EN media and the purely resistive nature of ENZ media. Moreover, this research proposes a theoretical framework for

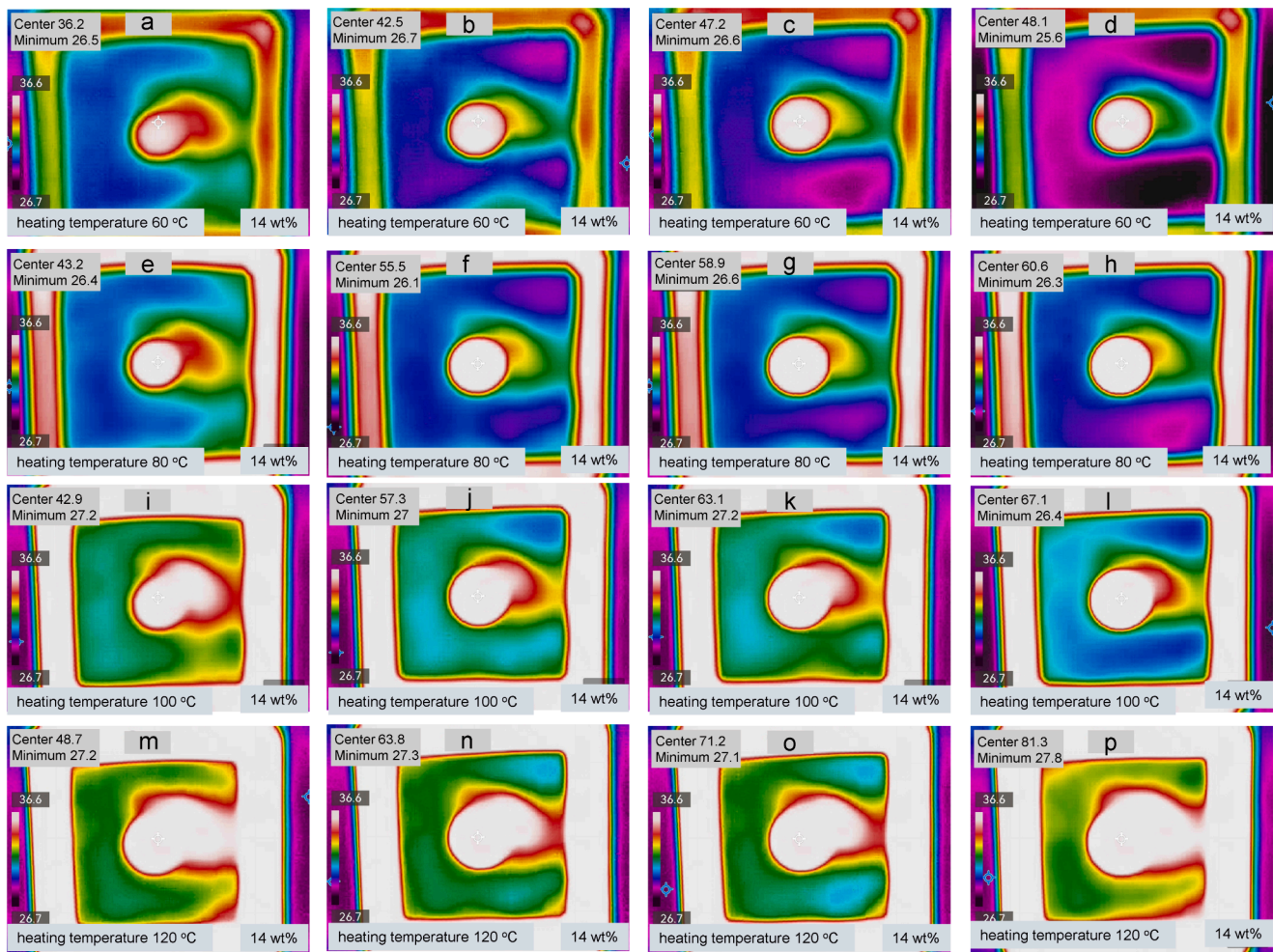


Fig. 6. Temperature pattern at heating temperature of (a-d) 60 °C, (e-h) 80 °C, (i-l) 100 °C and (m-p) 120 °C for metacomposites with MWCNT-CB content of 14 wt%. The interval between changes in each temperature field distribution map is five seconds.

designing an ideal EM shielding device using EN and ENZ media. By leveraging the synergistic effects of MWCNT-CB, this work introduces a new category of ternary metacomposites with tunable ENZ and EN responses, providing a foundational study for broadening the real-world applications of metacomposites and metamaterials in various fields.

CRediT authorship contribution statement

Yunpeng Qu: Writing – original draft, Conceptualization. **Yunlei Zhou:** Supervision, Conceptualization. **Farid Manshahi:** Writing – review & editing. **Kaidong Wang:** Writing – review & editing. **Chunyuan Deng:** Supervision. **Yao Liu:** Supervision.

Declaration of competing interest

The authors declare that they have no known competing financial interests or personal relationships that could have appeared to influence the work reported in this paper.

Data availability

Data will be made available on request.

Acknowledgements

This work was supported by the National Natural Science Foundation

of China [Grant No. 52205593], the Fund of Natural Science Special (Special Post) Research Foundation of Guizhou University [Grant No. 2023-032], and the Guizhou Provincial Basic Research Program (Natural Science) [Grant No. QianKeHeJiChu-ZK[2024]YiBan056].

Appendix A. Supplementary data

Supplementary data to this article can be found online at <https://doi.org/10.1016/j.compositesa.2024.108410>.

References

- [1] Zhang X, Jiang W, Jiang H, Wang Q, Tian H, Bai L, et al. An optically driven digital metasurface for programming electromagnetic functions. *Nat Electron* 2020;3: 165–71.
- [2] Lu X, Shapiro M, Mastovsky I, Temkin R, Conde M, Power J. Generation of high-power, reversed-Cherenkov wakefield radiation in a metamaterial structure. *Phys Rev Lett* 2019;122:014801–4.
- [3] Jahani S, Jacob Z. All-dielectric metamaterials. *Nat Nanotechnol* 2016;11:23–36.
- [4] Schurig D, Mock J, Justice B, Cummer S, Pendry J, Starr A, et al. Metamaterial electromagnetic cloak at microwave frequencies. *Science* 2006;314:977–80.
- [5] Smith D, Padilla J, Vier D, Nemat-Nasser S, Schultz S. Composite medium with simultaneously negative permeability and permittivity. *Phys Rev Lett* 2000;84: 4184–7.
- [6] Li X, Shi Z, Han M, Tang Q, Xie P, Fan R. All-polymeric multilayer para/ferroelectric dielectric films utilizing a gradient structure toward concurrent high discharge efficiency and energy density. *Mater Today Energy* 2022;29:101119.
- [7] Yin P, Xie P, Tang Q, He Q, Wei S, Fan R, et al. Enhanced dielectric energy storage properties in linear/nonlinear composites with hybrid-core satellite C/SiO₂@TiO₂ nanoparticles. *Appl Phys Lett* 2023;122:132905.

- [8] He Q, Sun K, Shi Z, Liu Y, Fan R. Polymer dielectrics for capacitive energy storage: from theories, materials to industrial capacitors. *Mater Today* 2023;68:298–333.
- [9] Zhu L, Yang Y, Li Y, Shi Z, Bie X, Yuan Y, et al. Remarkably enhancing dielectric permittivity and suppressing loss of PVDF via incorporating metal nanoparticles decorated glass fibers. *J Phys D: Appl Phys* 2024;57:205503.
- [10] Qu Y, Fan G, Liu D, Gao Y, Xu C, Zhong J, et al. Functional nano-units prepared by electrostatic self-assembly for three-dimension carbon networks hosted in $\text{CaCu}_3\text{Ti}_4\text{O}_{12}$ ceramics towards radio-frequency negative permittivity. *J Alloy Compd* 2018;743:618–25.
- [11] Qu Y, Du Y, Fan G, Xin J, Liu Y, Xie P, et al. Low-temperature sintering Graphene/ $\text{CaCu}_3\text{Ti}_4\text{O}_{12}$ nanocomposites with tunable negative permittivity. *J Alloy Compd* 2019;771:699–710.
- [12] Qu Y, Wu Y, Fan G, Xie P, Liu Y, Zhang Z, et al. Tunable radio-frequency negative permittivity of Carbon/ $\text{CaCu}_3\text{Ti}_4\text{O}_{12}$ metacomposites. *J Alloy Compd* 2020;834:155164.
- [13] Qu Y, Wu Y, Wu J, Sun K, Fan R. Simultaneous epsilon-negative and mu-negative property of Ni/ $\text{CaCu}_3\text{Ti}_4\text{O}_{12}$ metacomposites at radio-frequency region. *J Alloy Compd* 2020;847:156526.
- [14] Qu Y, Wang Z, Wang Z, Liu Y, Xie P, Wang Z, et al. Radio-frequency epsilon-negative property and diamagnetic response of percolative Ag/CCTO metacomposites. *Scripta Mater* 2021;203:114067.
- [15] Wang Z, Sun K, Xie P, Liu Y, Gu Q, Fan R, et al. Epsilon-negative BaTiO_3/Cu composites with high thermal conductivity and yet low electrical conductivity. *J Materiomics* 2020;6:145–51.
- [16] Shi Z, Fan R, Yan K, Sun K, Zhang M, Wang C, et al. Preparation of iron networks hosted in porous alumina with tunable negative permittivity and permeability. *Adv Funct Mater* 2013;23:4123–32.
- [17] Zhou Y, Qu Y, Yin L, Cheng W, Huang Y, Fan R. Coassembly of elastomeric microfibers and silver nanowires for fabricating ultra-stretchable microtextiles with weakly and tunable negative permittivity. *Compos Sci Technol* 2022;223:109415.
- [18] Leng Z, Yang Z, Tang X, Helal M, Qu Y, Xie P, et al. Progress in percolative composites with negative permittivity for applications in electromagnetic interference shielding and capacitors. *Adv Compos Hybrid Mater* 2023;6:195.
- [19] Qu Y, Lin J, Wu J, Wang Z, Sun K, Chen M, et al. Graphene-carbon black/ $\text{CaCu}_3\text{Ti}_4\text{O}_{12}$ ternary metacomposites toward a tunable and weakly epsilon-negative property at the radio-frequency region. *J Phys Chem C* 2020;124:23361–7.
- [20] Tang X, Zhang Z, Kuma D, Qu Y, Long Y, Xie P, et al. Flexible Carbon Nanotubes/Polystyrene membranous composites toward ultraweakly and frequency-stable negative permittivity at kHz region. *Eng Sci* 2023;24:920.
- [21] Yuan J, Zhou Y, Manshail F, Wang S, Yin J, Li D, et al. Ultraweakly low-dispersion epsilon-negative response of GR-CNT/PVDF ternary metacomposites. *Compos Commun* 2024;47:101877.
- [22] Cheng C, Wu Y, Qu Y, Ma R, Fan R. Radio-frequency negative permittivity of carbon nanotube/copper calcium titanate ceramic nanocomposites fabricated by spark plasma sintering. *Ceram Int* 2020;46:2261–7.
- [23] Qu Y, Cheng C, Ma R, Fan R. Spark plasma sintered GR-CNT/ $\text{CaCu}_3\text{Ti}_4\text{O}_{12}$ ceramic nanocomposites with tunable epsilon-negative and epsilon-near-zero property. *Ceram Int* 2021;47:17345–52.
- [24] Qu Y, Wu H, Xie P, Zeng N, Chen Y, Gong X, et al. Carbon nanotube-carbon black/ $\text{CaCu}_3\text{Ti}_4\text{O}_{12}$ ternary metacomposites with tunable negative permittivity and thermal conductivity fabricated by spark plasma sintering. *Rare Met* 2023;42:4201–11.
- [25] Qu Y, Xie P, Zhou Y, Ding J, Chen Y, Gong X, et al. Graphitized-MWCNT/ $\text{CaCu}_3\text{Ti}_4\text{O}_{12}$ metacomposites for tunable ϵ' -negative and ϵ'' -near-zero response with enhanced electromagnetic shielding. *Ceram Int* 2023;49:37407–14.
- [26] Qu Y, Peng Q, Zhou Y, Manshail F, Wang S, Wang K, et al. Fine-tunable ϵ' -negative response derived from low-frequency plasma oscillation in graphene/polyaniline metacomposites. *Compos Commun* 2023;44:101750.
- [27] Qu Y, Zhou Y, Luo Y, Liu Y, Ding J, Chen Y, et al. Universal paradigm of ternary metacomposites with tunable epsilon-negative and epsilon-near-zero response for perfect electromagnetic shielding. *Rare Met* 2024;43:796–809.
- [28] Qu Y, Hao M, Luan X, Yang Q, Ding J, Zhou L, et al. Regulation mechanism of epsilon-negative monolayer graphene/ $\text{CaCu}_3\text{Ti}_4\text{O}_{12}$ metacomposites for boosting electromagnetic shielding. *Adv Compos Hybrid Mater* 2024;7:38.
- [29] Guo Z, Sun Z, Wang P, Du B, Qian L. Dual Heteroatoms-Induced defect engineering in graphene towards metacomposites with epsilon-near-zero response. *Appl Surf Sci* 2023;638:158073.
- [30] Qu Y, Wang Z, Xie P, Wang Z, Fan R. Ultraweakly and fine-tunable negative permittivity of polyaniline/nickel metacomposites with high-frequency diamagnetic response. *Compos Sci Technol* 2022;217:109092.
- [31] Fan G, Feng T, Qu Y, Hao C, Liu Y. Dielectric properties and negative permittivity performance modulated by dual fillers in CNTs/TiN/ $\text{CaCu}_3\text{Ti}_4\text{O}_{12}$ ternary composites. *Ceram Int* 2022;48:28135–41.
- [32] Dai J, Luo H, Moloney M, Qiu J. Adjustable Graphene/Polyolefin elastomer epsilon-near-zero metamaterials at radiofrequency range. *ACS Appl Mater Interfaces* 2020;12:22019–28.
- [33] Swetha P, Aswini R, Binesh M, Muhammed T, Sridharan K, Swaminathan S. Cost efficient fabrication of flexible polymer metacomposites: impact of carbon in achieving tunable negative permittivity at low radio frequency range. *Mater Today Commun* 2023;34:105287.
- [34] Tian J, Fan R, Zhang Z, Li Y, Wu H, Yang P, et al. Flexible and biocompatible poly(vinyl alcohol)/multi-walled carbon nanotubes hydrogels with epsilon-near-zero properties. *J Mater Sci Technol* 2022;131:91–9.
- [35] Yao X, Kou X, Qiu J. Multi-walled carbon nanotubes/polyaniline composites with negative permittivity and negative permeability. *Carbon* 2016;107:261–7.
- [36] Luo H, Qiu J. Carbon Nanotube/Polyolefin elastomer metacomposites with adjustable radio-frequency negative permittivity and negative permeability. *Adv Electron Mater* 2019;5:1900011.
- [37] Sun K, Wang C, Tian J, Zhang Z, Zeng N, Yin R, et al. Magnetic-driven broadband epsilon-near-zero materials at radio frequency. *Adv Funct Mater* 2024;34:2306747.
- [38] Cheng C, Jiang Y, Sun X, Shen J, Wang T, Fan G, et al. Tunable negative permittivity behavior and electromagnetic shielding performance of silver/silicon nitride metacomposites. *Compos Part A-Appl S* 2020;130:105753.
- [39] Cheng C, Liu Y, Ma R, Fan R. Nickel/yttrium iron garnet metacomposites with adjustable negative permittivity behavior toward electromagnetic shielding application. *Compos Part A-Appl S* 2022;155:106842.
- [40] Fan G, Wang Z, Ren H, Liu Y, Fan R. Dielectric dispersion of copper/rutile cermets: dielectric resonance, relaxation, and plasma oscillation. *Scripta Mater* 2021;190:1–6.
- [41] Fan G, Wang Z, Zhang G, Liu Y, Fan R. Percolated cermets of nickel/yttrium iron garnet for double negative metacomposites. *Compos Commun* 2021;24:100667.
- [42] Yang P, Sun K, Wu Y, Wu H, Yang X, Wu X, et al. Negative permittivity behaviors derived from dielectric resonance and plasma oscillation in percolative bismuth ferrite/silver composites. *J Phys Chem C* 2022;126:12889–96.
- [43] Wei Z, Wang Z, Fan G, Xu C, Shi G, Zhang G. Low-frequency plasmonic state and negative permittivity in copper/titanium dioxide percolating composites. *Ceram Int* 2021;47:2208–13.
- [44] Ma R, Cheng C, Liu Y, Wang J, Zhou J, Hu Z, et al. Temperature dependence of negative permittivity behavior in graphene/alumina ceramic metacomposites. *J Eur Ceram Soc* 2024;44:3012–9.
- [45] Sun X, Cheng C, Shen J, Liu Y, Wang T, Ma Q, et al. Fine-tuning of negative permittivity behavior in amorphous carbon/alumina metacomposites. *Ceram Int* 2020;46:8942–8.
- [46] Liu Y, Cheng C, Sun W, Zhang Z, Ma R, Zhou J, et al. Negative permittivity behavior of carbon fibre/alumina ceramic composites prepared by hot-press sintering. *Ceram Int* 2022;48:10031–8.
- [47] Zhang Z, Liu M, Ibrahim M, Wu H, Wu Y, Li Y, et al. Flexible polystyrene/graphene composites with epsilon-near-zero properties 2022;5:1054–66.
- [48] M. Liu, H. Wu, Y. Wu, P. Xie, R. Pashameah, H. Abo-Dief, S. El-Bahy, Y. Wei, G. Li, W. Li, G. Liang, C. Liu, K. Sun, R. Fan, The weakly negative permittivity with low-frequency-dispersion behavior in percolative carbon nanotubes/epoxy nanocomposites at radio-frequency range, *Adv Compos Hybrid Ma*, 5 (2022) 2021–2030.
- [49] Sun K, Duan W, Lei Y, Wang Z, Tian J, Yang P, et al. Flexible multi-walled carbon nanotubes/polyvinylidene fluoride membranous composites with weakly negative permittivity and low frequency dispersion. *Compos Part A-Appl S* 2022;156:106854.
- [50] Jing T, Xu K, Wang Y, Xiang L, Tang B, Shi S, et al. In situ construction of high-thermal-conductivity and negative permittivity epoxy/carbon fiber@carbon composites with a 3D network by high-temperature chemical vapor deposition. *ACS Appl Mater Interfaces* 2023;15:54027–38.
- [51] Wang Z, Sun K, Wu H, Qu Y, Tian J, Ju L, et al. Epsilon-near-zero response derived from collective oscillation in the metacomposites with ultralow plasma frequency. *Compos Sci Technol* 2022;227:109600.
- [52] Qu Y, Zhou Y, Yang Q, Cao J, Liu Y, Qi X, et al. Lignin-derived lightweight carbon aerogels for tunable epsilon-negative response. *Adv Sci* 2024;11:2401767.